The Astrophysical Journal, 904:9 (14pp), 2020 November 20 https://doi.org/10.3847/1538-4357/abba39

Multiphase Circumnuclear Gas in a Low-β Disk: Turbulence and Magnetic Field Reversals

Yuki Kudoh[1,2], Keiichi Wada[1], and Colin Norman[3,4]
[1] Graduate School of Science and Engineering, Kagoshima University, Kagoshima 890-0065, Japan; k5751778@kadai.jp
[2] National Astronomical Observatory of Japan, Tokyo 181-8588, Japan
[3] Department of Physics and Astronomy, Johns Hopkins University, 3400 N. Charles Street, Baltimore, MD 21218, USA
[4] Space Telescope Science Institute, 3700 San Martin Drive, Baltimore, MD, 21218 USA
Received 2020 January 14; revised 2020 September 11; accepted 2020 September 16; published 2020 November 17

Abstract

We studied the magnetic field structures and dynamics of magnetized multiphase gas on parsec scales around supermassive black holes by using global 3D magnetohydrodynamics (MHD) simulations. We considered the effect of radiative cooling and X-ray heating due to active galactic nuclei (AGNs). The gas disk consists of a multiphase gas with (1) cold ($\leqslant 10^3$ K) and thin, and (2) warm ($\sim 10^4$ K) and thick components with a wide range of number densities. The turbulent magnetic energy at maximum is comparable to the thermal and turbulent kinetic energies in the turbulent motion. We confirmed that the turbulent velocity of the warm gas in the ambient cold gas is caused by magnetoconvective instability. The turbulent magnetic field due to magnetorotational instability (MRI) is developed in the disk, but the mean toroidal magnetic field dominates and supports in a quasi-steady state, where the plasma-β, the ratio between gas pressure and magnetic pressure, is low ($\beta < 1$). As often seen in adiabatic MHD simulations of rotating disks, the direction of the mean toroidal field periodically reverses with time even in multiphase gas structures. The direction reversal is caused by magnetic flux vertically escaping from the disk and by the combination of the MRI and the Parker instability.

Unified Astronomy Thesaurus concepts: Active galactic nuclei (16); Galaxy circumnuclear disk (581); Magnetohydrodynamics (1964); Galaxy nuclei (609)

Supporting material: animations

1. Introduction

Magnetic field plays a crucial role in gas dynamics and multiphase gas structures in the central regions of galaxies where various dynamical structures, such as outflows, jets, and turbulent motions of interstellar medium are present on a wide dynamic range from the accretion disk to kiloparsec scales. It is suggested that the magnetic field in the central region of our Galaxy is a few tens μG to mG (see, e.g., Ferrière 2009; Crocker et al. 2010; Han 2017). In particular, Hsieh et al. (2018) estimated the milligauss toroidal field and plasma-β, $\beta = 0.01$–1, where β is the ratio between thermal pressure and magnetic pressure,

$$\beta \equiv \frac{P_{\rm g}}{P_{\rm B}} = \frac{P_{\rm g}}{|\boldsymbol{B}|^2/2}. \quad (1)$$

Nishiyama et al. (2010, 2013) found that the mean toroidal field extends to scale heights with the galactic latitude $|b| < 0.^{\circ}4$ deduced from the Fe 6.7 keV line emission.

The circumnuclear magnetic field is also observed in some galaxies. In the prototypical type-2 Seyfert, NGC 1068, the polarimetry in the infrared suggested that the magnetic field is dominated by a toroidal field with a few tens of mG and $\beta \sim 0.15$ (Lopez-Rodriguez et al. 2015). Using the water vapor masers in NGC 4258 (Modjaz et al. 2005), the upper limit of the toroidal magnetic field $\sim$100 mG is inferred.

Global magnetohydrodynamic (MHD) simulations of a rotating gas disk suggested that a turbulent field is developed due to magnetorotational instability (MRI; Balbus & Hawley 1991). Using adiabatic MHD simulations for the Galactic center, Machida et al. (2009) and Suzuki et al. (2015) reported that magnetic turbulence is driven by MRI. Turbulence contributes to the angular momentum and mass transport in the disk. In the nonlinear phase of MRI, it is characterized by a quasi-periodic reversal of the direction of the mean toroidal field (e.g., Beckwith et al. 2011; O'Neill et al. 2011; Flock et al. 2012; Machida et al. 2013; Parkin & Bicknell 2013; Hogg & Reynolds 2016). This field reversal is caused by the vertical transport of the mean field buoyantly from the midplane. As a result, the amplification of the magnetic turbulence is saturated and, consequently, the field strength and the plasma-β in the midplane are limited in the nonlinear phase.

When $\beta \gtrsim 1$, the timescale of the direction reversal is often observed to be about 10 rotational periods. On the other hand, for $\beta < 1$, this timescale is longer in the nonlinear regime depending on β. Local 3D shearing box simulations reported that the reversal pattern is irregular for the isothermal stratified gas disk (Bai & Stone 2013; Salvesen et al. 2016b). They also showed that when $\beta \lesssim 0.4$, the field does not show reversal within 150 rotational periods. Using global MHD simulations, Zhu & Stone (2018) and Mishra et al. (2020) studied the MRI in a low-β disk. Contrary to local MHD simulations, the plasma-β is larger than unity at the midplane, and no field reversal is observed within 50 rotational periods. Fragile & Sądowski (2017) conducted simulations starting from a strong toroidal magnetic field ($\beta = 0.1$), and they found that magnetic field dissipates to $\beta \sim 10$ in a steady state after 10 rotational

periods. Salvesen et al. (2016a) pointed out that the poloidal field is necessary to form a strongly magnetized disk. Begelman & Pringle (2007) studied the low-β disk by compiling the typical unstable condition for MRI, and showed that even if there was no vertical magnetic field, the low-β MRI is limited by the unstable condition $\beta \gtrsim c_s/v_{\rm K}$, where $v_{\rm K}$ and c_s are the Keplerian and sound speeds, respectively. Therefore, for a given $v_{\rm K}$, the plasma-β driving MRI is determined by the disk temperature, and it is expected that an MRI with a low β can develop in a low-temperature gas disk.

In most of the previous global MHD simulations of the magnetic field in a rotating disk, the gas was assumed to be adiabatic; therefore, the multiphase nature of the magnetized gas was not well studied. However, the circumnuclear gas on parsec scales should consist of cold ($T \lesssim 10^3$ K), warm ($T \sim 10^4$ K), and hot ($T \gtrsim 10^5$ K) gases (see, e.g., for AGN: Netzer 2015, and for the Galactic center: Liu et al. 2013). Using global 3D simulations and considering radiative cooling and heating effects, Wada et al. (2009) and Wada (2012) showed that the gas inside tens of parsecs from SMBHs becomes multiphase. They applied their model to the circumnuclear disk in the Circinus galaxy, which is the nearest type-2 Seyfert galaxy, and found that the model is consistent with multi-wavelength observations (Wada et al. 2016), such as CO(3 − 2) and [CI](1 − 0) emission lines (Izumi et al. 2018; Wada et al. 2018). However, the magnetic field was not taken into account in their models.

There are several numerical studies for the magnetized circumnuclear gas on a parsec scale. Chan & Krolik (2017) and Dorodnitsyn & Kallman (2017) studied the evolution of warm gas with $\beta = 1$. However, the timescale of their simulations is about 10 rotational periods, which is not long enough for the magnetic field to become a steady state. The long-term steady-state behavior of the direction reversal of the mean magnetic field was not well studied. Moreover, MRI with low β in a nonlinear phase was not studied for the multiphase gases, especially below 10^4 K. For example, it is not clear whether turbulence is maintained even in the cold gas, and how different are the structures of the magnetic field compared with the adiabatic gas. The structure of the circumnuclear gas with a magnetic field should be important to consider the effect of the radiation feedback from the AGN. In order to clarify these questions, we study the long-term behavior of the strong magnetized gas around an SMBH by taking into account realistic cooling and heating processes.

This paper is organized as follows. In Section 2, we present the basic equation, initial condition, and numerical model. Cooling and heating processes are described in Section 2.1. Numerical results are shown in Section 3. Development of the MHD turbulence is show in Section 3.1. Time evolution of the mean toroidal magnetic field and the physical origin of the turbulence are discussed in Sections 3.2 and 3.3. The thermal structures of the magnetized multiphase gas are presented in Section 3.4. In Section 4, we discuss the direction reversal with low-β (Section 4.1) and the radiation pressure (Section 4.2). Finally, we summarize the results in Section 5.

2. Numerical Setup

2.1. Basic Equations

We study the parsec-scale magnetized gas disk using 3D MHD simulations, considering radiative cooling and various heating effects in the cylindrical coordinate (R, φ, z). The resistive MHD equations are:

$$\frac{\partial \boldsymbol{B}}{\partial t} + \boldsymbol{\nabla} \times \boldsymbol{E} = 0, \tag{2}$$

$$\frac{\partial \rho}{\partial t} + \boldsymbol{\nabla} \cdot [\rho \boldsymbol{v}] = 0, \tag{3}$$

$$\frac{\partial}{\partial t}(\rho \boldsymbol{v}) + \boldsymbol{\nabla} \cdot \left[\rho \boldsymbol{v}\boldsymbol{v} + \left(P_{\rm g} + \frac{B^2}{8\pi}\right)\mathbf{I} - \frac{\mathbf{B}\mathbf{B}}{4\pi}\right] = -\rho \boldsymbol{\nabla}\Phi, \tag{4}$$

$$\frac{\partial}{\partial t}\left(e + \frac{B^2}{8\pi}\right) + \boldsymbol{\nabla} \cdot [(e + P_{\rm g})\boldsymbol{v} - \boldsymbol{E} \times \boldsymbol{B}] = -\rho \boldsymbol{v} \cdot \boldsymbol{\nabla}\Phi - \rho \mathcal{L}(n, T), \tag{5}$$

$$e \equiv \frac{P_{\rm g}}{\gamma_{\rm g} - 1} + \frac{1}{2}\rho v^2, \tag{6}$$

where $\mathbf{I}$ denotes the unit tensor, $\boldsymbol{B}$ is the magnetic field, ρ is the gas density, $\rho \equiv m_{\rm H} n \sim m_{\rm H}(n_n + n_i)$ with number densities of neutral and ionized hydrogen. $P_{\rm g}$ is the thermal gas pressure. The gas temperature is adopted as that of an ideal gas with the specific heat ratio $\gamma_{\rm g} = 5/3$. The gravitational potential is assumed to be the Newtonian potential, $\Phi = GM_{\rm BH}/r$, where G is the gravitational constant, $M_{\rm BH} = 10^7 M_\odot$ is the mass of the SMBH, and $r = \sqrt{R^2 + z^2}$ is the distance from the SMBH. The electric field $\boldsymbol{E}$ obeys the Ohm's law, $\boldsymbol{E} = -\boldsymbol{v} \times \boldsymbol{B} + \eta \boldsymbol{\nabla} \times \boldsymbol{B}$. We assume the anomalous resistivity η as modeled by Yokoyama & Shibata (1994),

$$\eta = \begin{cases} \min\{\eta_{\rm max}, \eta_0(v_d/v_c - 1)^2\}, & v_d \geqslant v_c \\ 0, & v_d < v_c, \end{cases} \tag{7}$$

where $v_d = |\boldsymbol{\nabla} \times \boldsymbol{B}|/\rho$ is the electron–ion drift velocity, $v_c = 10^8$ cm s^{-1} is the critical velocity, and we adopted $\eta_0 = 10^{-9}$ and $\eta_{\rm max} = 10^{-6}$ pc^2 yr^{-1}, respectively. Note that the results presented below are not sensitive to η_0 and $\eta_{\rm max}$ (also see the Appendix).

The radiative cooling and heating term $\rho\mathcal{L}$ in Equation (5) is given as

$$\rho \mathcal{L} = n^2 \Lambda - n(\Gamma_{\rm UV} + \Gamma_{\rm X}), \tag{8}$$

where the cooling function Λ (Figure 1) is taken from Meijerink & Spaans (2005) and Wada et al. (2009). As a major heating source, we consider that X-ray photons come from the accretion disk, and the heating function is $\Gamma_{\rm X} = \Gamma_{\rm Coulomb} + \Gamma_{\rm Compton} + \Gamma_{\rm photoionic}$. The Coulomb interaction is given by

$$\Gamma_{\rm Coulomb} \equiv \eta_{\rm h} H_{\rm X} \text{ erg s}^{-1}, \tag{9}$$

where $\eta_{\rm h}$ is the efficiency in fixed 0.2, and $H_{\rm X}$ is the X-ray energy deposition rate, $H_{\rm X} = 3.8 \times 10^{-25}\xi$ erg s^{-1}. For the Compton and photoionization interactions, we use a formula given by Blondin (1994), i.e.,

$$\Gamma_{\rm Compton} \equiv 8.9 \times 10^{-36}\xi n(T_{\rm X} - 4T) \text{ erg s}^{-1}, \tag{10}$$

$$\Gamma_{\rm photoionic} \equiv 1.5 \times 10^{-21}(\xi n)^{1/4} n^{3/4} T^{-1/2} \times (1 - T/T_{\rm X}) \text{ erg s}^{-1}, \tag{11}$$

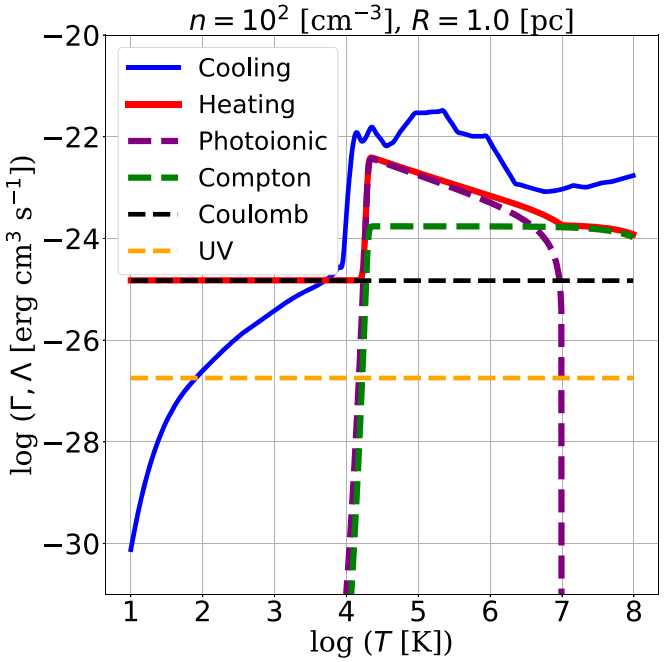

Figure 1. Cooling (blue) and heating (red) functions for $n = 10^2$ cm^{-3}. The total heating rate is decomposed with various sources: photoionization (purple), Compton (green), Coulomb collision (black), and UV radiation (yellow).

where $T_X = 10^8$ K is the characteristic temperature of an X-ray photon. Here the ionization parameter ξ is

$$\xi \sim 1.31 \times 10^2 \left(\frac{L_X}{10^{-4} L_{Edd}}\right)\left(\frac{r}{1\ \mathrm{pc}}\right)^{-2} \times \left(\frac{n}{10^2\ \mathrm{cm}^{-3}}\right)^{-1} \mathrm{erg\ cm\ s}^{-1}, \quad (12)$$

where L_X is X-ray luminosity and L_{Edd} is the Eddington luminosity for $M_{BH} = 10^7 M_\odot$. In this simulation, we set $\xi = 100$ for simplicity.

The photoelectric heating, assuming spatially uniform FUV is taken into account,

$$\Gamma_{UV} = 1.8 \times 10^{-25} \mathrm{erg\ s}^{-1}. \quad (13)$$

2.2. Initial Condition and Normalized Unit

We start the simulation from an equilibrium torus. In order to construct the equilibrium torus solutions with a toroidal field, we assume the polytropic relation,

$$P_g = K\rho^{\gamma_g}, \quad (14)$$

where K is the polytropic constant, and the weak toroidal field B_φ is given by plasma-β, $\beta = 100$. To give the density distribution, we assume the rotation velocity to be the radial distribution of angular momentum $L(R)$,

$$L(R) = L_0 \left(\frac{R}{R_0}\right)^a, \quad (15)$$

where $L_0 (\equiv R_0 v_0)$ and R_0 adopt the normalized units and $a = 0.35$ is the power index. The flux surface $\Psi(R, z)$ is then given as

$$\Psi(R, z) \equiv \Phi(R, z) + \frac{L^2(R)}{2(1-a)R^2} + \frac{1}{\gamma_g - 1} c_s^2(R, z) + \frac{\gamma_g}{2(\gamma_g - 1)} v_A^2(R, z), \quad (16)$$

where $c_s^2 = \gamma_g P_g / \rho$ is the square of the sound speed and $v_A^2 = B_\varphi^2/(4\pi\rho)$ is the square of the Alfvén speed. We defined the normalized unit as the torus density maximum, $\Psi_0 = \Psi(R_0, 0)$. For the condition of positive pressure, we can obtain a torus density distribution $\Psi(R, z) = \Psi_0$,

$$\rho_{torus}(R, z) = \rho_0 \left[\frac{\max\left\{\Psi_0 - \Phi(R, z) - \frac{L(R)^2}{2(1-a)R^2}, 0\right\}}{K\frac{\gamma_g}{\gamma_g - 1}(1 + \beta^{-1} R^{2(\gamma_g - 1)})}\right]^{1/(\gamma_g - 1)}. \quad (17)$$

We assume that the torus is embedded in the isothermal nonrotating and nonmagnetized halo, with pressure and density given by

$$P_{g,\,h} = K_h \rho_h, \quad (18)$$

$$\rho_h = 10^{-5} \rho_0 \exp\left[-\{\Phi(R, z) - \Phi(R_0, 0)\}/K_h\right]. \quad (19)$$

The normalized quantities are listed in Table 1. The polytropic indexes K and K_h are parameterized by the square of the velocity ratio, $\varepsilon = K\rho_0^{\gamma_g - 1}/v_0^2 = \gamma_g^{-1} c_s^2(R_0, 0)/v_0^2$ in the normalization, and we set $\varepsilon = 0.04$ in the torus and $\varepsilon_h = 2$ in the halo, respectively.

Table 1
Normalization

Quantity	Unit	Definition	Normalization
Central BH Mass	$M_\odot$	M_{BH}	$10^7 M_\odot$
Length	R_0	⋯	1 pc
Velocity	v_0	$\sqrt{GM_{BH}/R_0}$	2.07×10^7 cm s^{-1}
Time	t_0	R_0/v_0	4.74×10^3 yr
Density	ρ_0	⋯	1.673×10^{-22} g cm^{-3}
Pressure	P_{g0}	$\rho_0 v_0^2$	7.16×10^{-8} erg cm^{-3}
Temperature	T_0	$v_0^2 m_p/k_B$	5.19×10^6 K
Magnetic Field	B_0	$\sqrt{4\pi\rho_0 v_0^2}$	949 μG

2.3. Numerical Methods and Model Setup

We use CANS+ code (Matsumoto et al. 2019), which is implemented using the HLLD solver (Harten–Lax–van Leer discontinuitues; Miyoshi & Kusano 2005) with div B cleaning (Dedner et al. 2002) and three-stage total variation diminishing Runge–Kutta time integration (TVDRK). The fifth-order accuracy in space is achieved through the Monotonicity Preserving method (MP5; Suresh & Huynh 1997) to capture small-scale magnetic fluctuations. Basic equations are solved using conservative forms with geometrical and gravitational source terms explicitly included. After TVDRK updating, the cooling and heating source terms are treated in the implicit operator splitting approach.

As a numerical constraint in our simulation, we set the floor of the gas pressure in the grid cells where the minimum temperature is $T = 20$ K or the minimum plasma-β is

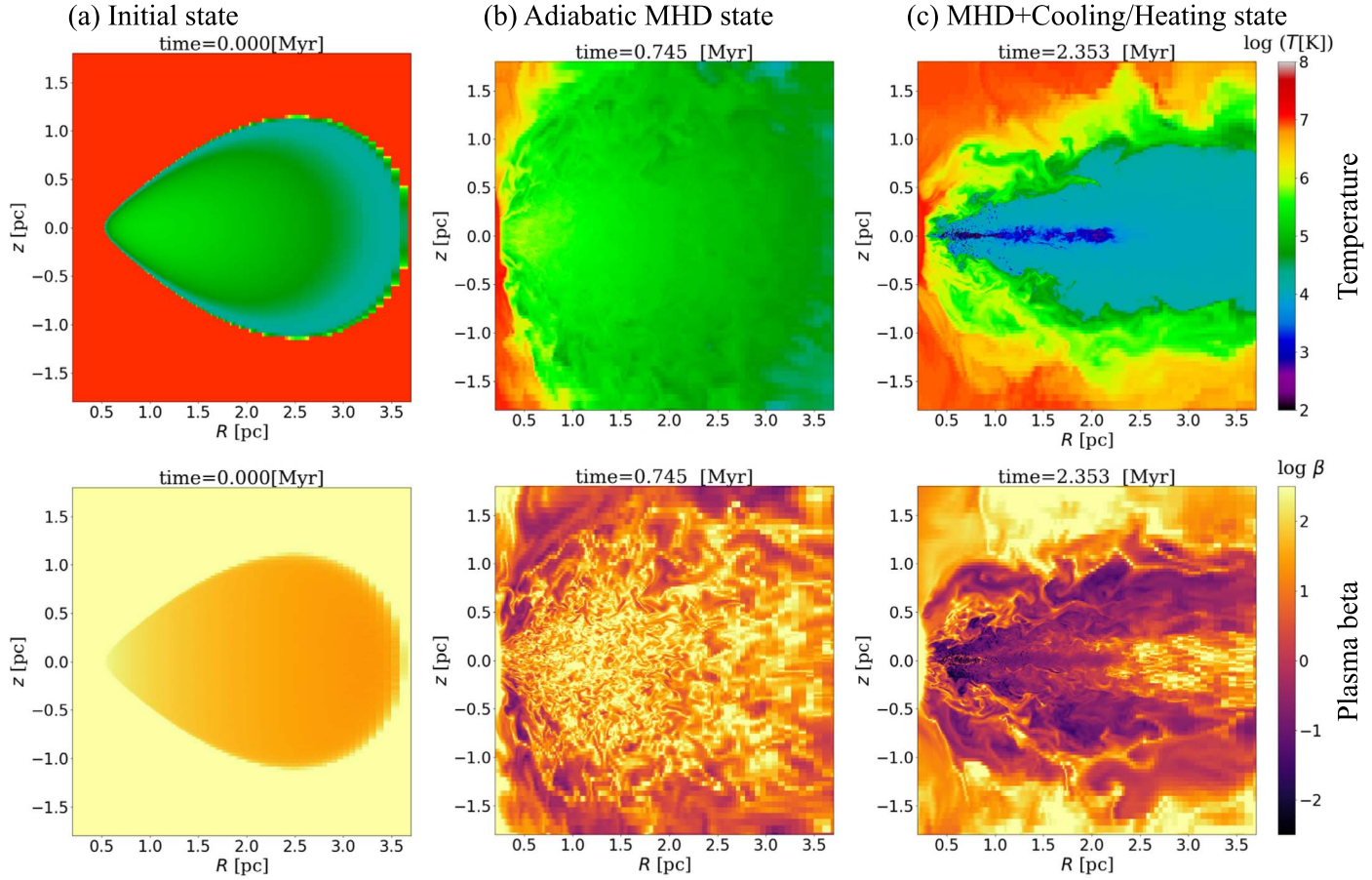

Figure 2. Snapshots of temperature and plasma-β in the R–z plane. Panels from left to right denote (a) initial state at $t = 0.000$ Myr, (b) adiabatic MHD evolution at $t = 0.744$ Myr, and (c) MHD including cooling and heating effects at $t = 2.353$ Myr. Associated with these snapshots we show an animation with temperature (top) and plasma-β (bottom). The animation runs from $t = 0.000$ to $t = 3.639$ Myr.

(An animation of this figure is available.)

$\beta = 0.001$. Comparing the volume-averaged energies of the grid cells where the lower limit is applied, the thermal energy is always 2–3 orders of magnitude smaller than the kinetic and magnetic energies. This implies that the artificial thermal energy due to the numerical floor does not affect the gas dynamics.

The size of the simulation box is $0 \leqslant R/R_0 < 12$, $0 < \varphi$ [rad] $< 2\pi$, $|z/R_0| < 3$. The grid size is $\Delta R = 0.01R_0$ and $\Delta z = 0.002R_0$. We use a coarser grid size outside for $R/R_0 > 2.0$ or $|z/R_0| > 0.4$, and for the region around the axis $R/R_0 < 0.2$. The numbers of grid cells are $N_R = 256$, $N_\varphi = 512$, and $N_z = 512$.

We assume the outflow boundary condition for the outer boundaries (i.e., $R/R_0 = 10$ and $|z|/R_0 > 2.8$). For the azimuthal direction, the periodic boundary condition is assumed. Meshes around the cylindrical axis are sent to the opposite computational domain of the azimuthal direction, which means that fluid can flow across the polar axis ($R = 0$). In the central region for $r/R_0 < 0.4$, we impose an absorbing boundary condition, i.e.,

$$q_{\rm new} = q - D(q - q_{\rm init}), \tag{20}$$

where q and $q_{\rm init}$ are the primitive variables of the TVDRK updating state and the initial state, respectively. Damping function $D(r)$ is modeled as,

$$D(r) = 0.1\left[1 - \tanh\left(\frac{r - 0.2R_0}{0.01R_0}\right)\right]. \tag{21}$$

We start the simulations assuming the adiabatic MHD, then after the magnetic field strength sufficiently develops and the system becomes a quasi-steady state at $t \leqslant 0.477$ Myr (25 rotational periods at $R = 1$ pc), the cooling and heating terms are considered until $t \leqslant 3.64$ Myr (97 rotational periods).

3. Results

3.1. Development of the MHD Turbulence in the Torus

Figure 2 shows three snapshots ($t = 0.000$, 0.744, and 2.353 Myr) of the gas temperature and the plasma-β on a R–z plane. Figure 2(a) shows the initial conditions. As explained in Section 2.3, the system evolves adiabatically until $t = 0.477$ Myr. During this period, gas spreads out vertically, and intense magnetic field fluctuations are developed by the MRI and $\beta > 0.6$ inside the torus. The magnetic field is stronger near the surface of the torus with $\beta \sim 0.2$. MRI causes not only turbulent motion but also heating due to magnetic reconnection. After cooling and heating are taken into account, the structure of the torus changes (Figure 2(c)). The plasma-β around the midplane becomes smaller with $0.003 < \beta < 6.0$. The torus becomes geometrically thinner, and it consists of two

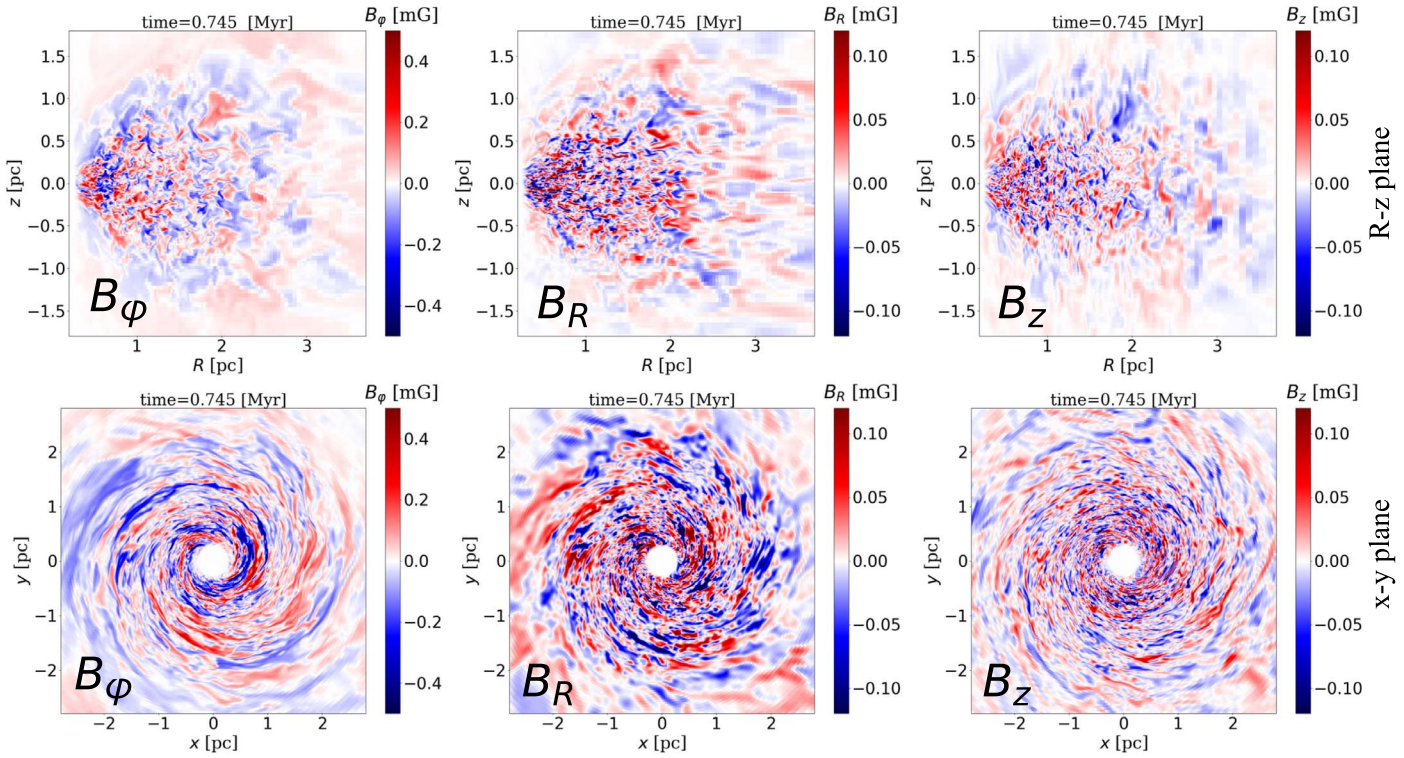

Figure 3. Adiabatic MHD state of magnetic field distributions in the x–y plane of $z = 0$ (top) and the R–z plane of $\varphi = 0$ (bottom) at $t = 0.744$ Myr. From left to right, field components are toroidal, radial, and vertical fields. Blue and red colors denote the negative and positive signs, respectively, for these right-handed coordinates.

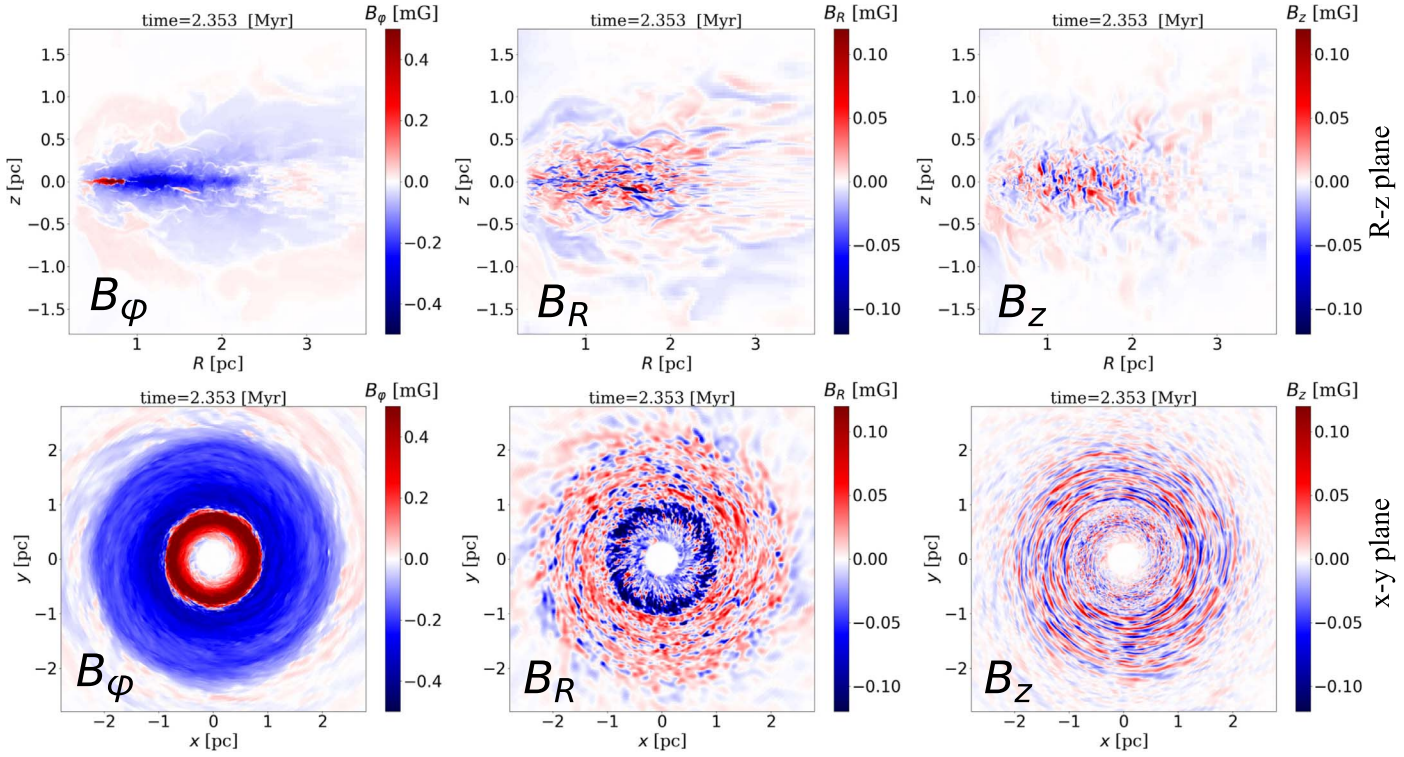

Figure 4. Same snapshots as in Figure 3, but for the calculation of MHD with cooling/heating effects at $t = 2.353$ Myr. This figure is available as an animation, running from $t = 0.744$ to $t = 3.642$ Myr.

(An animation of this figure is available.)

components: cold disk ($T \lesssim 10^3$ K) and warm disk ($T = 10^{3-5}$ K). The cold, thin disk ($R < 2$ pc) is supported vertically by the magnetic field as discussed below.

Figure 3 shows the magnetic field structure at $t = 0.744$ Myr of the adiabatic MHD state. The turbulent field in the torus dominates in the R–z and R–φ planes. The toroidal field (B_φ)

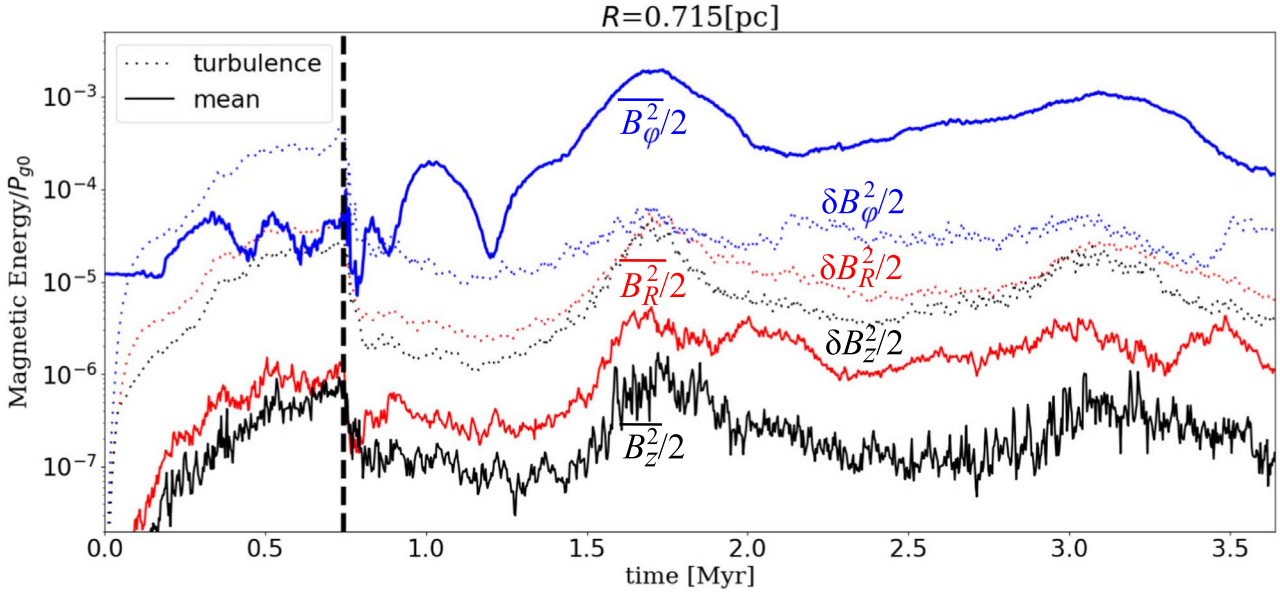

Figure 5. Time evolution of magnetic field energy separated into mean field ($\overline{B_i}^2/2$ where $i = R, \varphi, z$) and turbulent field ($\delta B_i^2/2$). Each energy measures the volume weighted average over a ring of a rectangular cross section; $0.715 - \Delta R/2 \leqslant R$ pc $< 0.715 + \Delta R/2$, $0 \leqslant \varphi$ rad $< 2\pi$, and $|z|$ pc $\leqslant 1$. The dashed vertical line at $t = 0.744$ Myr is the turning point of the states between the adiabatic MHD (left side) and MHD+cooling/heating (right side). Colors denote the toroidal component (blue), the radial component (red), and the azimuthal component (black).

shows the flux bundle of the positive direction (red) around the torus surface at $|z| = 1.5$ pc.

Figure 4 is the same as Figure 3, but cooling and heating are considered ($t = 2.353$ Myr). The field strength and turbulent fluctuation are markedly different from those in Figure 3. The toroidal field B_φ dominates the total magnetic field. The two plots of B_φ show that the mean toroidal field has more coherent structures compared to that in the adiabatic phase (Figure 3) with opposite directions shown in blue and red in Figure 4. On the other hand, radial and vertical magnetic fields are dominated by the turbulent component. We can also see that the patches of B_R and B_z with opposite directions tend to extend radially and vertically, respectively.

For a more quantitative observation, we decomposed the magnetic energy into mean and turbulent components. We measured the mean component as the azimuthal average,

$$\overline{f}(R, z, t) \equiv \frac{1}{2\pi}\int_0^{2\pi} d\varphi f(R, \varphi, z, t). \quad (22)$$

Hence, the turbulent component is derived as,

$$\delta f(R, \varphi, z, t) \equiv f(R, \varphi, z, t) - \overline{f}(R, z, t), \quad (23)$$

where we notate the mean as ¯ and the turbulence as δ. Figure 5 shows the evolution of the magnetic energy in each component. It is clear that the structures of the magnetic field change drastically after the cooling and heating. For $t < 0.5$ Myr, turbulent fields become exponentially stronger than mean fields, while the ratios between them are approximately constant, i.e., $\delta B_\varphi^2/\delta B_R^2 \sim 10$ and $\delta B_\varphi^2/\delta B_z^2 \sim 22$. After cooling/heating at $t = 0.744$ Myr, the turbulent fields decrease quickly by one order of magnitude, and they survive until $t \sim 3.5$ Myr. This turbulent field dissipation is caused by the decrease in the gas temperature (see in Section 4). During this phase, we found that $|\delta B_\varphi| > |\delta B_R| > |\delta B_z|$, but the ratios between them change.

In the adiabatic MHD state, the amplitude of $\overline{B_\varphi}$ (blue solid line in Figure 5) reaches a quasi-steady state with a periodical cycle of $T_{\rm cycle} = 0.163$ Myr ~9.1 rotational periods. After cooling/heating effects are included, oscillating amplification of $\overline{B_\varphi}$ continues for $0.744 < t < 1.75$ Myr. The quasi-steady state is achieved when $\overline{B_\varphi}$ does not significantly change . However, $|\overline{B_\varphi}|$ shows quasi-periodic oscillations on a long timescale beyond reaching steady state. This amplitude and period become larger and longer than those of the adiabatic MHD state. Around the maximum of $|\overline{B_\varphi}|$ (i.e., $t = 1.75$, 3.08 Myr), $|\delta \boldsymbol{B}|$ and $|\overline{B_R}|$ are maximized, and around the minimum of that (i.e., $t = 2.1$, 3.2 Myr), $|\delta \boldsymbol{B}|$ and $|\overline{B_R}|$ are maximized. We show the quasi-periodic spatial changing in the animation of Figure 4.

Steady-state behavior is also seen from examining the mass flux inside 0.9 pc for $t > 1.75$ Myr. The radial profile of the net mass accretion rate appears to be roughly constant in time, which has been observed in simulation studies (e.g., Stone & Pringle 2001; Jiang et al. 2019). We took the time averages over 1.6 Myr, which is the longest timescale in the periodic oscillation of $|\overline{B_\varphi}|$. The time variation of the mass accretion rate due to MRI turbulence has been discussed in O'Neill et al. (2011), Hawley et al. (2011), and Hogg & Reynolds (2016). Since the mass flux varies with the averaging time interval, the time domain $0.744 < t < 1.75$ Myr is not steady.

3.2. Direction Reversal and Vertical Transport

The periodical cycle of the mean toroidal field energy is observed to have the pattern of a quasi-periodic direction reversal. Figure 6 (top), the so-called butterfly diagram, is the space (z-direction) time evolution of the mean toroidal field direction at $R = 0.715$ pc. It shows that the direction periodically changes at a given z, and it also implies that the B-field escapes from the midplane. Figure 6 (bottom) is for the mean plasma-β, $\overline{\beta} \equiv 2\overline{P_{\rm g}}/|\overline{\boldsymbol{B}}|^2$. The disk surface traces the bounding surface for $\overline{\beta} \leqslant 10$. This implies that the magnetic

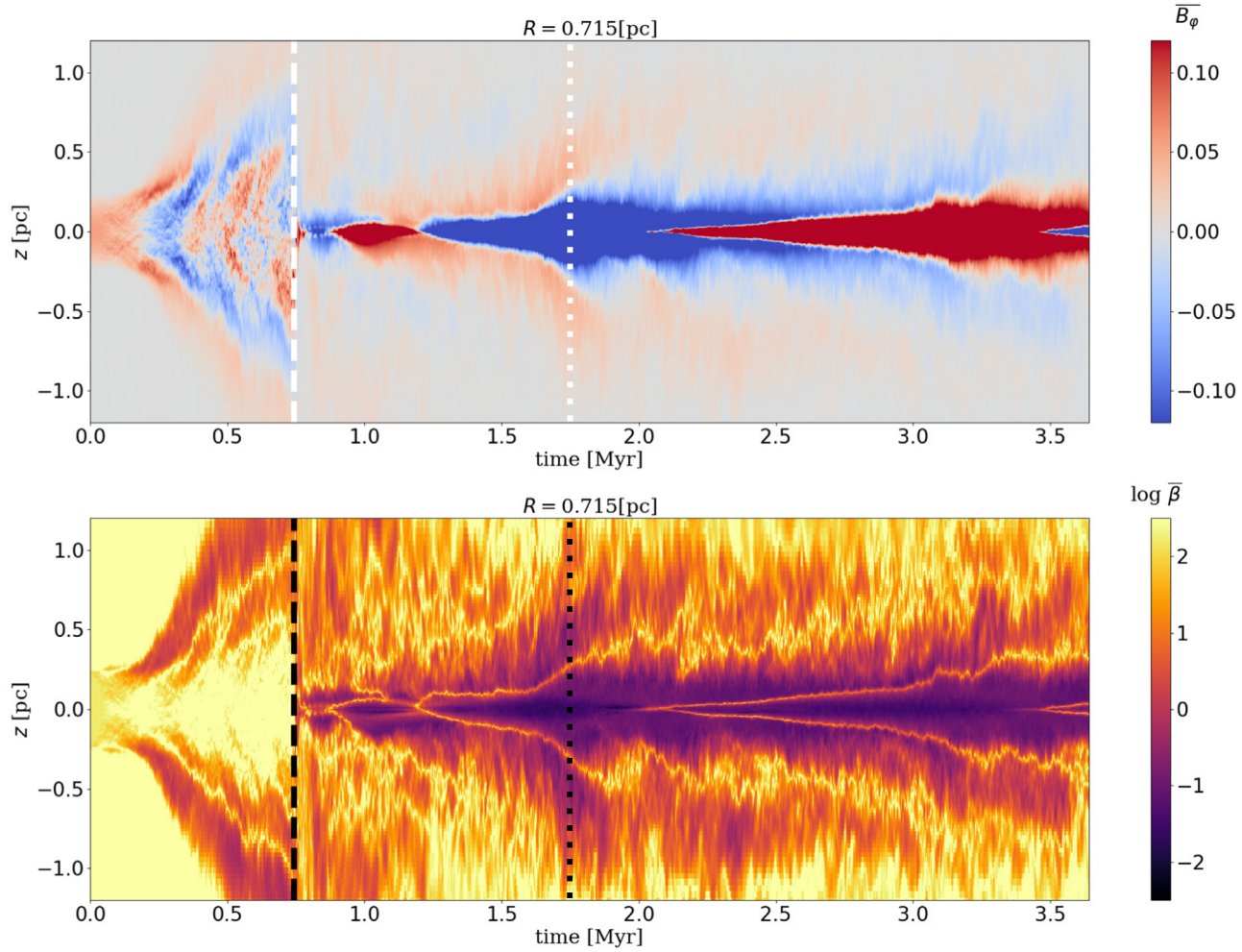

Figure 6. Space–time diagrams at $R = 0.715$ pc. Top panel is the mean of the toroidal field and the bottom panel is the mean plasma-β. Dashed vertical line at $t = 0.744$ Myr is the turning point between the adiabatic MHD (left side) and MHD+cooling/heating (right side). Dotted vertical line in each panel at $t = 1.75$ Myr is when the system becomes a quasi-steady state.

field becomes amplified near the midplane and is transferred to the high latitudes of the disk. The quasi-steady radial mass flow indicates the saturation of the MRI-driven turbulence.

In the MHD+cooling/heating state ($t > 0.744$ Myr), the lowest plasma-β is in the midplane, and mean field transport is slower than that of the adiabatic MHD. The direction of B_φ in $1.20 < t$ Myr < 2.27 is vertically stratified in blue around the midplane and red above that. The vertical transport changes from slow to fast at time $t = 1.74$ Myr. Recall that the energy of B_φ increases and decreases in Figure 5, and this time is the maximum point. The same phenomenon occurs on the next reversal where it is red around the midplane and blue above that. We have confirmed the cycle through the mean toroidal field direction reversal and escape from the disk.

The vertical escape of the mean field is described as the vertical magnetic energy transport using the Poynting flux $F_{P,z}$,

$$F_{P,z} = B_R(v_z B_R - B_z v_R) - B_\varphi(v_\varphi B_z - B_\varphi v_z), \tag{24}$$

$$\overline{v_B} \equiv \frac{\overline{F_{P,z}}}{\overline{B}_\varphi^2}, \tag{25}$$

where a rise speed v_B denotes the vertical derivative of the pattern of the mean toroidal field (Salvesen et al. 2016b). The large rise speeds occur at the direction reversal, and large fall speeds appear around the midplane and $|z| > 0.5$ pc (Figure 7). The maximum rise speed v_B is 37.3 km s^{-1} in $|z| < 0.8$ pc. In the same way, Alfvén speed and vertical speed are measured as $|v_A| \sim 41.6$ km s^{-1} and $|v_z| \sim 44.0$ km s^{-1}, and these speeds are comparable. The rise speed cannot reach the gravitational escape speed, 244.8 km s^{-1} at $R = 0.715$ pc.

3.3. Turbulent Velocity Field and Magnetoconvective Instability

In this subsection, we investigate the physical origin of the turbulent magnetic field shown in Section 3.1 and how it is maintained. Figure 8 shows the turbulent velocity field of the gas at $t = 2.353$ Myr. The maximum upflow (blue arrows) is about 18% of the escape velocity at that position. The gas circulates with downward and upward flows in the ambient, where $\log\{P_g/(\gamma_g - 1)\} \lesssim -4$. The velocity inside the disk is relatively smaller than that in the ambient. The magnitude of the turbulent velocity for $R \lesssim 0.9$ pc is comparable to the sound speed. That for $R \gtrsim 0.9$ pc is roughly 10% of the sound speed. The direction of vectors does not coincide with the turbulent and mean magnetic fields; however, part of the gas falls into the midplane along the magnetic field lines. Each component of the turbulent field and velocity has a difference only within one order of magnitude.

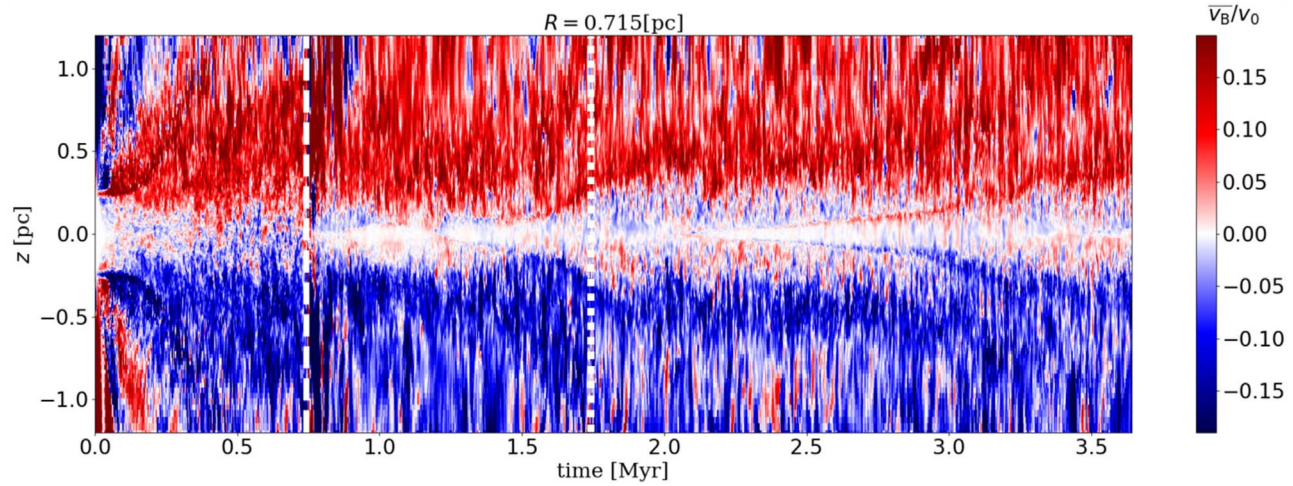

Figure 7. Same as Figure 6, but for the mean rise speed ($\overline{v_B}/v_0$) of the toroidal magnetic flux at $R = 0.715$ pc. Red and blue denote the positive speed and negative speed for the vertical direction, respectively.

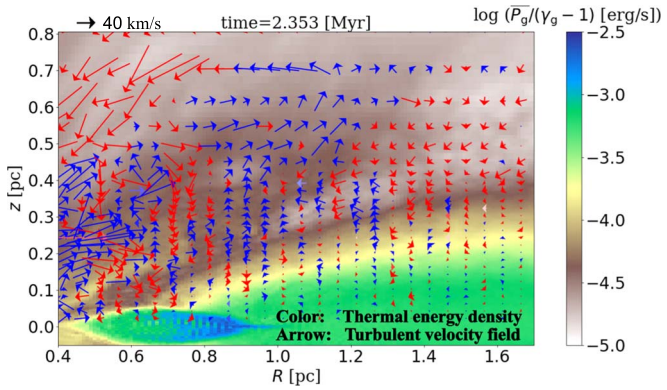

Figure 8. Turbulent velocity field (i.e., deviation from the mean velocity field) and mean thermal energy density distributions in the R–z plane at the same time as the right panels of Figure 2. The arrows above $z = 0$ are colored blue for $\delta v_z > 0$, and red for $\delta v_z < 0$. (For reference, a velocity of 40 km s^{-1} is shown on the top left.)

Figure 9 shows the vertical structures of the magnetic, thermal, and kinetic energies at a given radius at $t = 2.533$ Myr. Around the midplane, the mean toroidal magnetic field dominates the turbulent magnetic and kinetic energies ($\overline{\rho}\,\overline{|\delta \boldsymbol{v}|^2}/2$), both of which are comparable to the thermal energy ($\overline{P_g}/(\gamma_g - 1)$). The mean field decreases more rapidly than the turbulent component with z. As a result, there are regions where $\overline{\delta B_\varphi^2} > \overline{B}_\varphi^2$ ($0.2 \lesssim |z|$ pc $\lesssim 0.8$). The transition between the turbulent component and the mean field also occurs at the disk surface ($|z| \sim 0.05$ pc), where the mean field reverses its direction as seen in Figure 6. At higher latitude ($|z| \gtrsim 0.3$ pc), contrary to the midplane ($z = 0$ pc), turbulent toroidal field energy ($\overline{\delta B_\varphi^2}/2$) is about 10% of the mean thermal energy, but it is comparable to or a few times larger than the kinetic energy.

The vertical random motion could be related to the magnetoconvective instability (or interchange instability, see, e.g., Acheson 1979). The unstable criterion is

$$\frac{d}{dz}\left(\frac{P_B}{\rho^{\gamma_B}}\right) = \frac{d}{dz}\left(\frac{B_\varphi^2/2}{\rho^2}\right) < 0 \text{ (unstable)}. \tag{26}$$

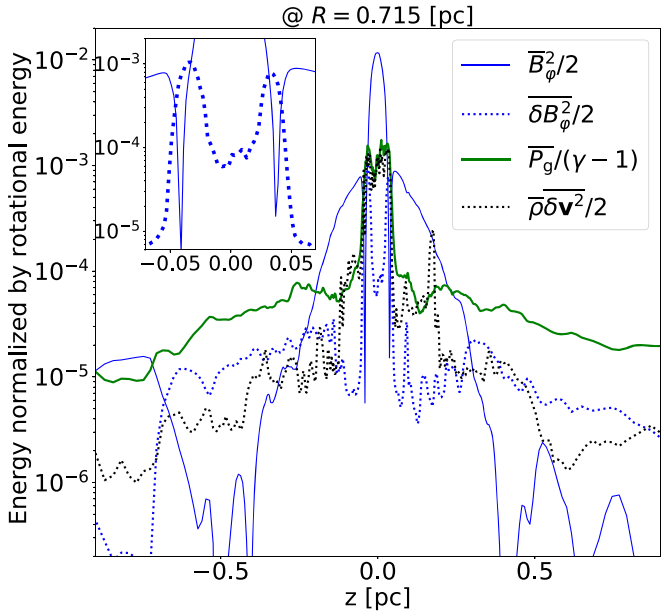

Figure 9. Vertical distribution of mean energy densities in the MHD+cooling/heating state at $t = 2.353$ Myr. The mean energy density in the turbulent fields δB_i^2 and $\rho \delta v_i^2$ ($i = R, \varphi, z$) is averaged over the azimuthal direction. Normalized energy densities are the rotational energy, $\rho_0 v_K/2$, estimated by substituting the number density $n = 10^2$ cm^{-3} and Keplerian rotation v_K at $R = 0.715$ pc. Colors represent the thermal energy (green), the turbulent kinetic energy (black), and the toroidal magnetic energy (blue). Dotted and solid lines denote the turbulent and mean components.

This criterion corresponds to the convective instability for the gas with decreasing specific entropy s with large $|z|$, i.e.,

$$\frac{ds}{dz} \propto \frac{d}{dz}\left(\frac{P_g}{\rho^{\gamma_g}}\right) < 0 \text{ (unstable)}. \tag{27}$$

Replacing P_g and γ_g in the relation (27) with P_B and γ_B, where the magnetic pressure $P_B = |\boldsymbol{B}|^2/2$, the criterion (26) is obtained. Here $\gamma_B = 1 + P_B/U_B = 2$ for the energy density $U_B = |\boldsymbol{B}|^2/2$ (e.g., Kulsrud 2005). The criterion (26) can be written as $d(|B_\varphi|/\rho)/dz < 0$. Therefore, the instability occurs when the mass frozen in the magnetic flux tube per unit length increases with increasing $|z|$.

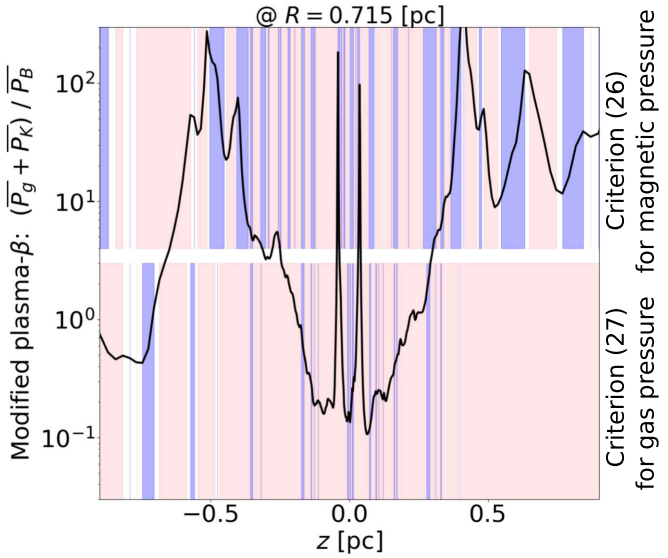

Figure 10. Vertical distribution of the mean modified plasma-β (solid line) and the criterion of convective instabilities (shadows) at $t = 2.353$ Myr. The mean modified plasma-β represents $(\overline{P_g} + \overline{P_K})/\overline{P_B}$, where P_K is the ram pressure evaluated by the turbulent kinetic energy, $\rho|\delta \boldsymbol{v}|^2$. The vertical distribution stability is shaded in red, and the unstability in blue. Stability evaluation is performed using the gradient of the mean quantities from Equation (26) (upper) and Equation (27) (lower).

One should note that the criteria (27) and (26) are necessary conditions for convection. We compare the two criteria with the vertical variation of the modified plasma $\hat{\beta}$, i.e., $\hat{\beta} \equiv (\overline{P_g} + \overline{P_K})/\overline{P_B}$ in Figure 10, where $P_K \equiv \overline{\rho}\delta \boldsymbol{v}^2$. Note that the strong ram pressure exists around the midplane, and $P_K \sim P_g$, but magnetic energy dominates. In the bottom panel of Figure 10, hydrodynamic convection is essentially stable, i.e., the positive entropy gradient shown in red shadows. In contrast, as seen in the top panel of Figure 10, there are many unstable regions for the magnetoconvective instability (blue shadows). From the conditions, i.e., $\frac{d}{dz}\left(\frac{P_B}{\rho^2}\right) < 0$(unstable), $\frac{d}{dz}\left(\frac{P_g}{\rho^{\gamma_g}}\right) > 0$(stable), after some algebraic calculations to vanish the density gradient, we can derive

$$\frac{1}{P_B}\frac{dP_g}{dz} + \frac{\gamma_g}{2}P_g\frac{d}{dz}\left(\frac{1}{P_B}\right) > 0. \tag{28}$$

When $d|B_\varphi|/dz \sim 0$ (i.e., when field direction reversal occurs) and/or $\gamma_g/2 \sim 1$, this condition satisfies $d\beta/dz > 0$. Figure 10 shows that the regions with $d\hat{\beta}/dz > 0$ correspond to unstable regions for magnetoconvective instability.

The two panels of Figure 11 show the unstable regions for the two criteria, (26) and (27). They show that the unstable regions for the magnetoconvection form belt-like layers, where the mean toroidal field direction reverses (see, B_φ on the R–z plane in Figure 4). The unstable layers move with the rising direction pattern of the mean toroidal field. The width of the unstable layers remains approximately constant around 0.05–0.1 pc. The bottom panel implies that the system is convectively stable.

3.4. Thermal State of the Magnetic Activity

Figure 12 shows the vertical distributions of the density and temperature at $R = 0.715$ pc at $t = 2.353$ Myr. For $|z| < 0.05$

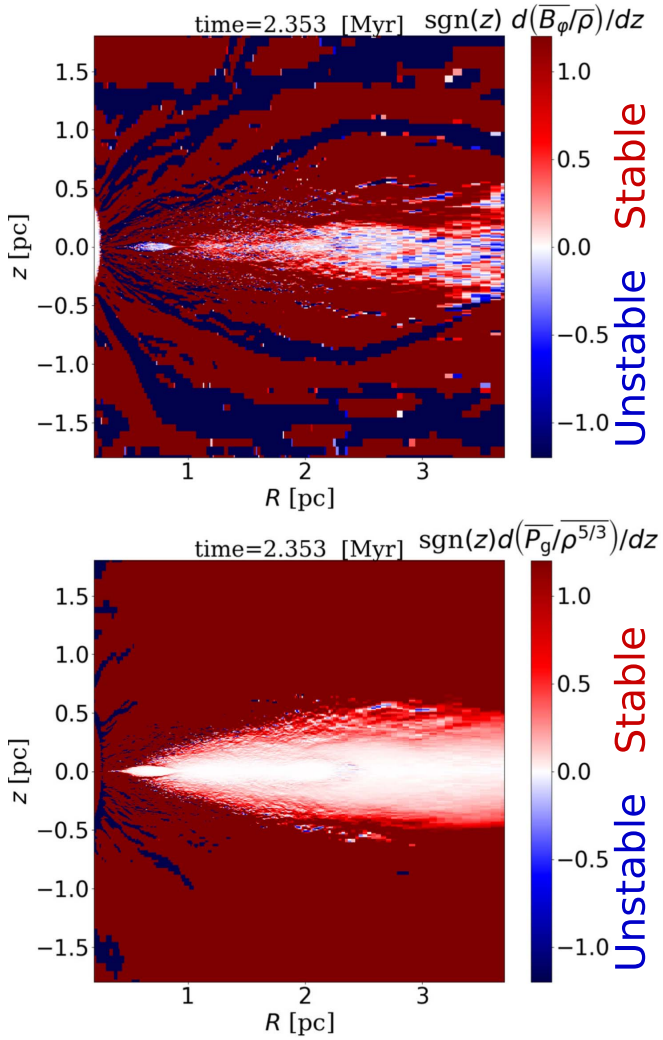

Figure 11. Stability of convective instabilities in the R–z plane at $t = 2.353$ Myr. Top: magnetoconvection of Equation (26). Bottom: hydrodynamic convection of Equation (27). Blue and red denote the same criteria as in Figure 10.

pc, the gas is cold ($\sim 8 \times 10^2$ K) and dense ($n \sim 10^3$ cm^{-3}). As seen in Figure 2(c), this cold disk extends to $R \sim 2$ pc. Outside this cold, dense disk, the gas is warm ($\sim 10^4$ K) and less dense ($n \sim 10$ cm^{-3}); therefore, they are roughly in pressure equilibrium. The temperature of the ambient region ($|z| > 0.25$ pc) increases continuously until $\sim 10^6$ K. Figure 12 also shows that there is a large azimuthal fluctuation around the mean values. The density fluctuation is in the order of unity or less while the temperature, as a maximum, fluctuates by three orders of magnitude. For the cold disk ($|z| < 0.05$ pc), the minimum temperature reaches the lower limit, and the maximum does not exceed 10^4 K of the warm disk.

To quantify the temperature and density fluctuations in phase space, we plot the gas mass fraction as a function of gas pressure and number density in the top panel of Figure 13. A large amount of gas mass is collected in characteristic regions over the gas mass fraction $\log(M/M_{\rm tot}) > -5$. These are multiphase states created by the thermal instability. The gas is also distributed in a wide range of densities and temperatures, but a large fraction of the gas is in a state with $P_g/k_B \gtrsim 10^5$ and $n \gtrsim 1$. The bottom panel in Figure 13 shows the spatial distributions of four thermal states shown in the top panel on

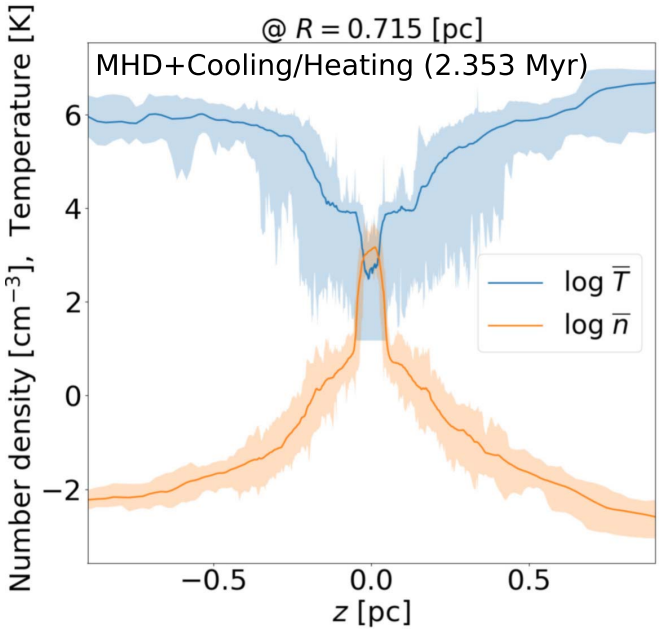

Figure 12. Vertical distribution of the temperature (blue) and the number density (red) at $R = 0.715$ pc of the MHD+cooling/heating state $t = 2.353$ Myr. Shadowed areas are the maximum and minimum values over the toroidal direction. Solid lines are the azimuthally averaged density and temperature.

the R–z plane. The colors represent the region enclosed by the same colors on the P_g–n plane. The low-temperature gases are patchy in the warm ($\sim 10^4$ K) thick disk shown in blue. The mass fraction of this low-temperature gas is small. Although the mass fraction of gas in the red region is small, The green region refers to the dense gas in a cold ($\sim$100 K) phase. The gas shown in yellow in the top panel mostly forms the thick disk at $R > 0.9$ pc as shown in the bottom panel, where they are approximately isothermal (therefore, the gas pressure is constant).

In Figure 14, density and temperature for $R < 0.9$ pc (i.e., the quasi-steady cold, thin gas disk) are plotted as functions of the magnetic pressure P_B and the thermal pressure P_g at $t = 2.35$ Myr. In the region where magnetic pressure dominates ($\beta < 1$), the number density of the left panel is distributed in a wide range from $n \sim 10^{-2}$ to 10^4 cm^{-3} for a given gas pressure. It shows that the temperature is lower than $T \sim 10^5$ K, and the strongly magnetized gas consists of cold gas with $T < 1000$ K, which dominates the total mass (Figure 13). In the high-β domain, the temperature and density fixed at gas pressure are not sensitive to changes in magnetic field. The thermal state is determined by the compression and expansion of the gas pressure.

In the above results, we observe a thin cold ($T < 100$ K) disk where the magnetic field is strong ($\beta \lesssim 1$) at $R < 0.9$ pc (see Figures 13 and 14). This structure is stable at least until the end of the simulation, i.e., $t \sim 3.6$ Myr ($\sim$96 rotational periods at $R = 1$ pc). The disk is maintained by the MRI and by the mass inflow from the outer disk ($R > 0.9$ pc), where the gas is less dense and less magnetized. Therefore, we suspect that this strongly magnetized disk is not transient, and it could last during the lifetime of the AGNs ($\sim$10 Myr).

If this is the case, a strong magnetic field at $R < 1$ pc could be expected in AGNs, and it can be observable by the Zeeman effect using future observations by ALMA, ng-VLA, and SKA.

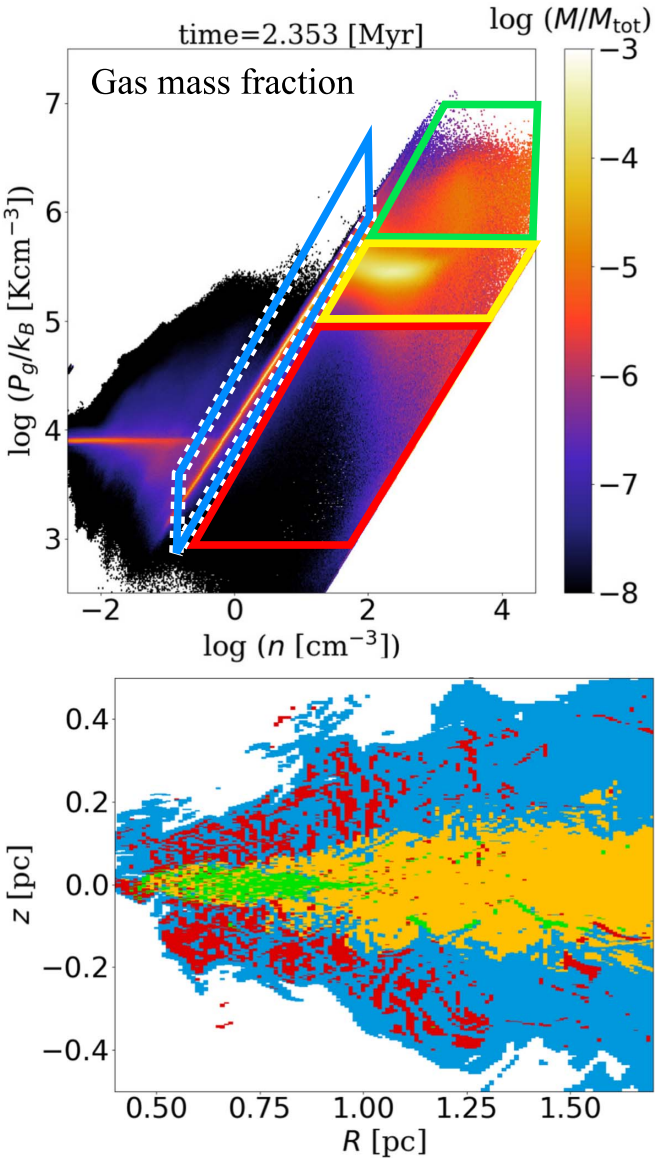

Figure 13. Top panel is a 2D histogram with the gas pressure in the vertical axis and the number density in the vertical axis at $t = 2.352$ Myr. Color contour denotes the mass fraction distribution occupying cells of $\Delta(\log n) = \Delta(\log P_g/k_B) = 0.01$ and averaged over the number of mesh points in each P_g–n space cell. Bottom panel is the R–z plane distribution corresponding to some regions enclosing each color in the top panel. Light blue: $3.4 < \log\ (T[\mathrm{K}]) < 4.6$, $-1 < \log\ (n[\mathrm{cm}^{-3}]) < 2$; red: $2.0 < \log T < 3.4$, $3 < \log(P_g/k_B[\mathrm{Kcm}^{-3}]) < 5$; yellow: $1 < \log T < 3.4$, $5 < \log(P_g/k_B) < 5.8$; and green: $1 < \log T < 3.6$, $5.8 < \log(P_g/k_B) < 6.8$. Note that the gas temperature denotes a constant slope as $d\log(P_g/k_B)/d\log n$, assuming the ideal gas.

If the mass supply from the outer region is stopped, the magnetic field can be dissipated by the ambipolar diffusion (see, Equation (A10) and the Appendix). The expected timescale is

$$t_{\mathrm{Adiff}} \sim Re_{\mathrm{M,A}} \frac{L}{V} \sim 3.8\ \mathrm{Myr} \left(\frac{x}{10^{-4}}\right) \times \left(\frac{B}{1\mathrm{mG}}\right)^{-2} \left(\frac{n_n}{10^4 \mathrm{cm}^{-3}}\right)^2 \left(\frac{L}{1\mathrm{pc}}\right)^2, \quad (29)$$

which is still long enough to be observed.

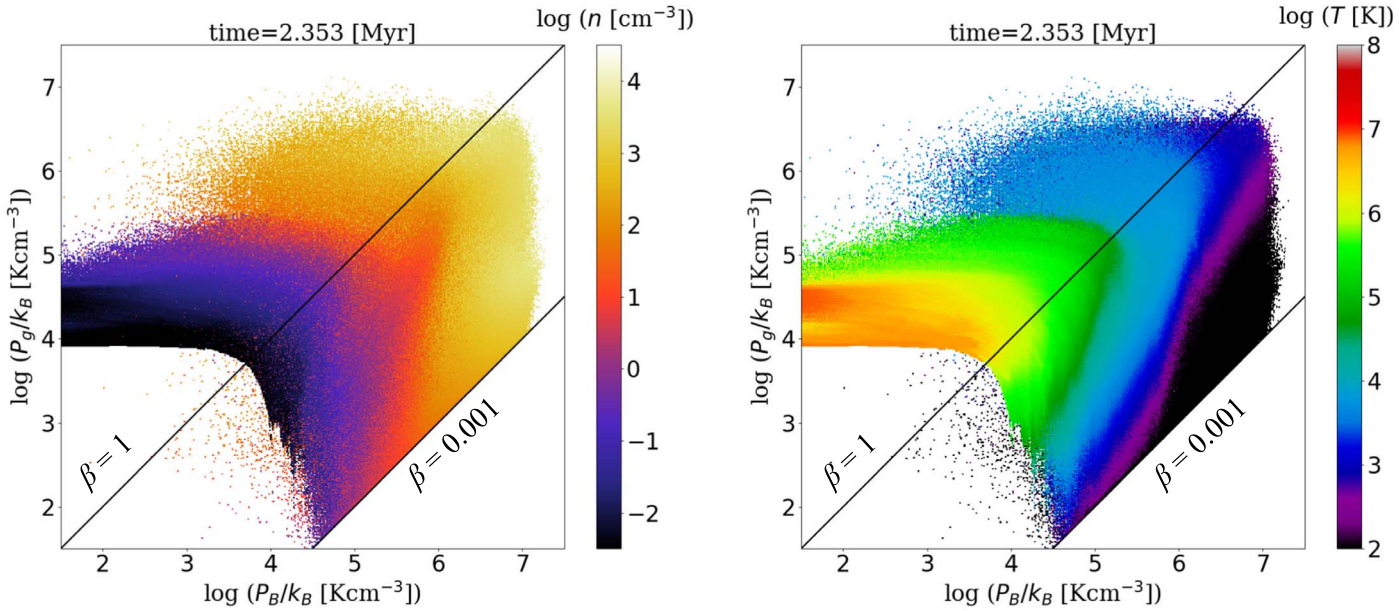

Figure 14. Two-dimensional histograms of the gas pressure in the vertical axis and the magnetic pressure in the horizontal axis inside $R = 0.9$ pc at $t = 2.352$ Myr. Left: number density. Right: temperature. Occupying cells are $\Delta(\log P_g/k_B) = \Delta(\log P_B/k_B) = 0.01$. Solid lines are $\beta = 1.000$ and 0.001 (lower limit).

4. Discussion

4.1. Direction Reversal in the Low-β MRI

We found that the low-β disk formed by radiative cooling and heating is discernible by the direction reversal (Figure 6) and vertical transfer of the magnetic field (Figure 7). A long reversal period is observed in the strong toroidal field with low β compared to the turbulence with high β. This trend is also found in the local 3D simulations of an isothermal gas (Bai & Stone 2013; Salvesen et al. 2016b). The mean plasma-β, $\overline{\beta} \sim$ 0.1–0.4 in the midplane is also similar to our result (see, Figure 10; Table 2 of Salvesen et al. 2016b). Compared to an analytical model (Begelman et al. 2015), it was demonstrated that heating efficiency, defined as the ratio between the dissipation rate (e.g., the magnetic reconnection) and mean toroidal field production rate, decreases with β. Salvesen et al. (2016b) showed that assuming steady Poynting flux, the period of the direction reversal is proportional to the rotational period ($T_{\rm cycle} = 2\pi/\Omega\xi_B^{-1}$) and is determined by the phenomenological parameters; $\xi_B = \nu\eta_B/(\beta - \nu + 1)$, where $\nu_B = \eta_B\Omega z$ (see also Equation (25)) and ν is the degree of turbulent heating. The turbulent heating caused by the nonlinear MRI is weakened by the small plasma-β (see, Table 3 of Salvesen et al. 2016b).

The field direction reversal as seen in Figure 6 is caused by the changes in balance between the turbulent energy and the mean field energy. When the direction of the mean field, which is represented by two shaded colors, reverses (e.g., $t = 1.20$, 2.12, 3.48 Myr in Figure 15), the energy density $\overline{B}_\varphi^2/2$ (blue solid line) temporarily drops and the turbulent magnetic field ($\delta\boldsymbol{B}_\varphi^2/2$; blue dotted line) is amplified. While the turbulent kinetic energy ($\overline{\rho}\delta\boldsymbol{v}^2/2$; black dotted line) exceeds the thermal energy ($\sim P_{\rm g}$; green solid line), the turbulent magnetic energy (blue dotted line) is smaller than the thermal energy of cold gas ($T \sim 1000$ K), i.e., β at this moment becomes large. The direction reversal is caused by a combination of MRI and the Parker instability (Figure 16 or see, e.g., Machida et al. 2013). A magnetic field line with a small radial fluctuation (panel (a)) is stretched to the radial and azimuthal directions (panel (b)). The stretched field line with a longer wavelength is selectively buoyed up toward higher latitudes by the Parker instability (panel (c)). As a result, for the R–φ plane, the buoyant field line has an opposite direction to the field line in the midplane. In the low-β disk, direction reversal is possible by driving turbulence from the mean field; thus, the process to high β will be important (i.e., magnetoconvection in Section 3.3). Direction reversal was widely observed in adiabatic MHD simulations (e.g., Beckwith et al. 2011; O'Neill et al. 2011; Flock et al. 2012; Machida et al. 2013; Parkin & Bicknell 2013; Hogg & Reynolds 2016), but we found here for the first time that *direction reversal also occurs in the low-β disk with the multiphase gas* ($10 < T$ [K]$<10^5$).

We observed the strongly magnetized disk driven by MRI in Section 3. We discuss here what constrains the strength of the magnetic field (plasma-β) in this simulation. In Figure 10, the mean plasma-β around the cold disk shows $\bar{\beta} > 0.1$. This satisfies the condition for the MRI, i.e., $\bar{\beta} > \beta_{\rm crit}$ (Begelman & Pringle 2007), above which the MRI can be driven, and

$$\beta_{\rm crit} \sim 0.01\left(\frac{T}{1000{\rm K}}\right)^{1/2}\left(\frac{v_{\rm K}}{253{\rm kms}^{-1}}\right)^{-1}. \quad (30)$$

where we adopted the Keplerian rotation v_K at $R = 0.715$ pc and the mean temperature in Figure 12. On the other hand, the mean plasma-beta is expressed as $\bar{\beta}^{-1} \sim (\delta B_\varphi^2/2 + \overline{B_\varphi}^2/2)/P_{\rm g}$. For $\overline{B_\varphi}^2 \geqslant \delta B_\varphi^2$, which is the case in the disk, $\bar{\beta} \leqslant P_{\rm g}/\delta B_\varphi^2$. From Figure 15, $P_{\rm g}/\delta B_\varphi^2 \sim 10$; therefore, the mean plasma-beta can be constrained as $0.01 \lesssim \bar{\beta} \lesssim 10$.

It has been known that the MRI-driven turbulence depends on numerical spatial resolution. Hawley et al. (2011, 2013) applied the quality factor $Q_\varphi \equiv \lambda/(R\Delta\varphi)$, which is the resolution of the characteristic MRI wavelength ($\lambda = 2\pi B_\varphi/\sqrt{\rho\Omega^2}$). They identified the empirical condition as $Q_\varphi \gtrsim 20$. However, for the toroidal field, the numerical convergence of adiabatic turbulence has not been clarified yet.

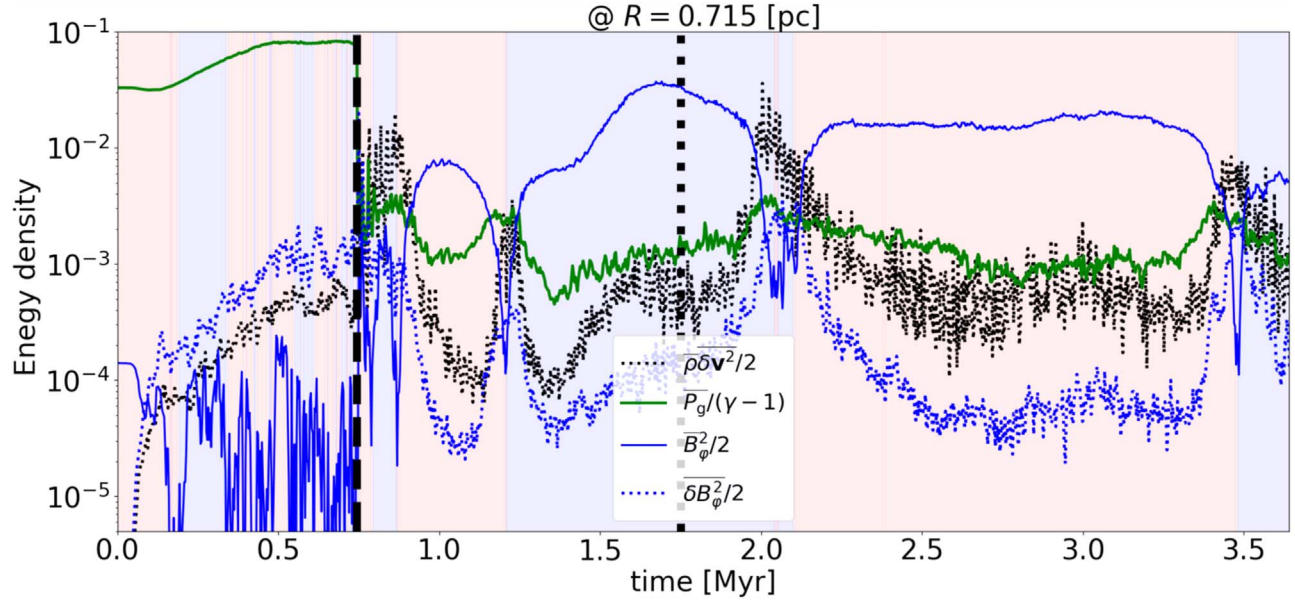

Figure 15. Time variation of the energy densities in the midplane at $R = 0.715$ pc. Each energy density is normalized by the rotational energy with a density of ρ_0 and Keplerian rotation at a radius of $R = 0.715$ pc. Solid and dotted lines represent the energy density of the mean and turbulent components, respectively. Different colors of solid lines denote the mean toroidal B-field energy (blue), the mean thermal energy (green), and the turbulent kinetic energy (gray). Shaded colors of red and blue signify the direction of the mean toroidal field.

The low-β MRI in cold gas requires high resolution,

$$Q_\varphi \sim 32\left(\frac{N_\varphi}{512}\right)\left(\frac{v_\varphi}{207\ \mathrm{km\ s^{-1}}}\right)^{-1}\left(\frac{T}{100\ \mathrm{K}}\right)^{1/2}\left(\frac{\beta}{10^{-2}}\right)^{-1/2}, \tag{31}$$

where $N_\varphi = 2\pi/\Delta\varphi$ is the azimuthal resolution. In our model, $N_\varphi = 512$ and we found that $Q_\varphi \gtrsim 20$ (see, e.g., Kudoh & Wada 2018). Additionally, a comparison with $N_\varphi = 128$ showed that the low resolution is $Q_\varphi < 10$, and thus, there is no direction reversal in the cold and low-β disk. Our simulations are in agreement with the estimation of Equation (31) and the empirical condition. In the long-term calculation, the turbulent magnetic field is sensitive to the numerical flux solver and the high-order accuracy. In order to reduce numerical dissipation, HLLD flux solver is employed (see, e.g., Hawley et al. 2013). Matsumoto et al. (2019, e.g., Section 3.2.1; 4.3) pointed out that the high-order accuracy prevents the dissipation rather than the low-order scheme. We took a highly precise numerical approach, hence the differences from previous global 3D simulations.

4.2. Radiation Pressure

AGNs emit enormous energy fluxes over a wide wavelength, and its feedback is important for the dynamics of the circumnuclear gas (e.g., Chan & Krolik 2016, 2017). However, IR radiative pressure is not dynamically effective (Namekata & Umemura 2016), and cannot contribute to MRI in the cold gas. Notably, the anisotropic radiation pressure on the dust in the gas with the X-ray heating produces flows in a fountain-like manner in the central tens-of-parsec regions around the AGNs (Wada 2012). The radiation pressure is expected to be stronger than the magnetic pressure, i.e.,

$$\begin{aligned}\frac{P_{\rm rad}}{P_B} &\sim \frac{mnL_{\rm X}\kappa_d\alpha_d/(cR)}{B_\varphi^2/2}\\ &\sim 3\left(\frac{L_{\rm X}}{10^{-4}L_{\rm Edd}}\right)\left(\frac{\kappa_d\alpha_d}{10^3\ \mathrm{cm^2 g^{-1}}}\right)\\ &\times\left(\frac{n}{10^3\ \mathrm{g\ cm^{-3}}}\right)\left(\frac{R}{1\ \mathrm{pc}}\right)^{-1}\left(\frac{B_\varphi}{1\ \mathrm{mG}}\right)^{-2},\end{aligned} \tag{32}$$

where $\kappa_d = 10^5$ is the dust opacity and $\alpha_d = 0.01$ is the gas to dust ratio (Wada 2012). In a subsequent paper, we will investigate the effect of radiation pressure, how magnetic structures are changed, and how magnetic buoyancy or magnetoconvection can help.

5. Summary

We studied the evolution of a magnetized multiphase gas using global 3D MHD simulations in the parsec-scale galactic nuclei. The simulation starts from an adiabatic state ($\mathcal{L} = 0$ in Equation (5)) with a weak toroidal field, $\beta = 100$, until the MHD turbulence is fully developed ($\beta \sim 0.6$) for $\sim$25 rotational periods (0.744 Myr) at $R = 1$ pc. Thereafter, the effects of the radiative cooling and the X-ray heating from the accretion disk around the SMBH are taken into account for an additional 97 rotational periods (2.89 Myr). The quasi-steady state in a time sufficiently longer than the dynamical timescale is attained in the radii $R < 0.9$ for $t > 1.75$ Myr, as confirmed by a time variation of the mean toroidal field and a constant of the accretion rate averaged over variation timescale.

Major findings are:

(i) The cold ($<10^3$ K) gas forms a geometrically thin disk around the midplane. The warm ($\sim 10^4$ K) gas forms a thicker disk, and the hot ($\sim 10^6$ K) gas is distributed to higher latitudes (Figures 12, 13). The mass fraction ($>10^{-5}$) on the $P_{\rm g}$–n plane is in the warm and cold phases (Figure 13). The magnetic

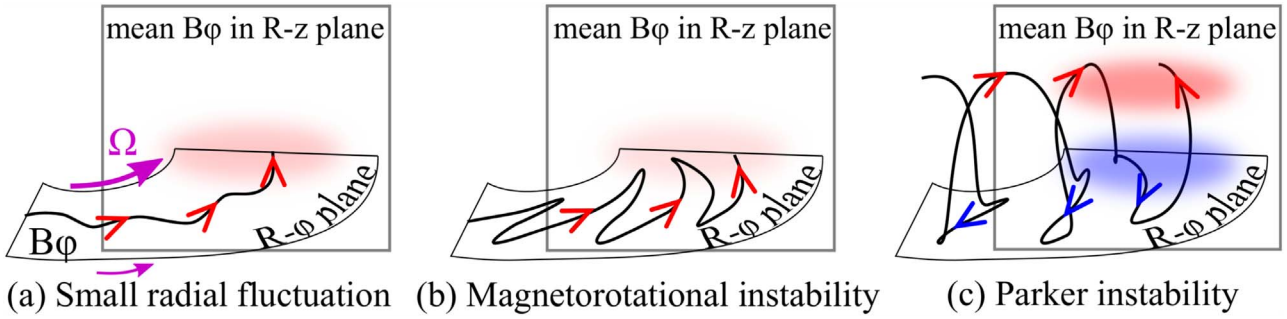

Figure 16. Schematic illustration of the MRI-Parker dynamo in the differential rotational disk. A magnetic field line is drawn as black curves with colored arrows. Red and blue arrows signify parallel and antiparallel and the purple arrows indicate the rotational direction. (a) A magnetic field line is threaded by the toroidal field with a small radial turbulence on the R–φ plane at a certain height; (b) MRI and disk rotation stretch the magnetic field line to the radial and toroidal direction in the R–φ plane; (c) Parker instability buoyantly escapes from the R–φ plane of (a).

pressure is stronger (i.e., β (<1)) in the cold, dense gas (Figure 14).

(ii) The mean magnetic field is dominated by a toroidal component, and a strongly magnetized cold disk with $\beta \sim 0.02$ is formed (Figures 2, 3, and 4). The mean toroidal field moves with the cold gas to a radial and vertical direction. The energy of the turbulent field is suppressed by the cooling effect; however, it is always comparable to or smaller than the thermal energy (Figures 5 and 15).

(iii) The turbulent motion in the multiphase gas is observed in the R–z plane (Figure 8). Magnetoconvective instability plays a key role in maintaining turbulence for a long period. The unstable condition $d(|\overline{B}_\varphi|/\rho)/dz < 0$ (Equation (26)) coincides with the region in the modified plasma-β increasing vertically upward (Figure 9) and in the belt-like mean field reversal in the R–z plane (Figure 11). The transition between the turbulent component and the mean field also occurs at the disk surface ($|z| \sim 0.05$ pc and $0.2 \lesssim |z|$ pc $\lesssim 0.8$), where the mean field spatially reverses its direction (Figures 4 and 9).

(iv) The quasi-steady state differs for the plasma β inside the disk. The high-β disk is achieved by the saturation of $|\delta \boldsymbol{B}|^2$ and the oscillation of $\overline{B}_\varphi^2$ (Figure 5). In our simulations starting from the initial weak toroidal field ($\beta = 100$), the magnetic field strength amplified by the MRI remains $\beta \gtrsim 1$ and the oscillation timescale is about 10 rotational periods, as mentioned in the previous studies. The quasi-steady state in the low-β disk is obtained by the periodic change of $\overline{B}_\varphi^2$. The period in the low-β state is more than 5 times longer (about 50 rotational periods) than that found in the high-β state.

(v) We found that even for low-β (~ 0.02), the mean toroidal field shows direction reversals with time (Figures 5 and 6). This is caused by the transportation of the magnetic field vertically due to Parker instability (Figure 16), similar to the adiabatic state. The direction reversal of the mean B_φ occurs, when the turbulent magnetic energy becomes larger than mean magnetic energy (Figure 15). The moving speed of the magnetic field (Equation (25)) estimated by the Poynting vertical flux is about 10% of the rotation speed. This speed becomes a maximum where the mean toroidal field direction reverses (Figure 7). To continue this cycle, mean magnetic flux transport from midplane to vertical direction is important.

Additional Links

Movies of snapshots of Figures 2 and 4 are available in the following link https://astrophysics.jp/MHD_torus/.

The authors are grateful to the anonymous referee for constructive comments and suggestions. We thank Ryoji Matsumoto, Mami Machida, and Yusuke Tsukamoto for their constructive comments and discussion, and the CANS+ developer team for the numerical techniques. Numerical computations were performed on Cray XC50 and XC30 systems at the Center for Computational Astrophysics, National Astronomical Observatory of Japan. This work was supported by JSPS KAKENHI grant No. 16H03959 and by NAOJ ALMA Scientific Research grant No. 2020-14A.

Appendix
Nonideal MHD effects

In this paper, we solved ideal MHD equations, whereby the gas in the circumnuclear region moves together with the magnetic field. This would be justified because we assumed that the ionization degree is ($x \equiv n_i/n_n$), $x \sim 10^{-4}$ following Meijerink & Spaans (2005). However, this assumption is incorrect if the magnetic Reynolds numbers for the dissipation processes in terms of the ohmic effect, Hall effect, and ambipolar diffusion being smaller than unity. Here, we confirm this.

The electric field in the induction equation (Equation (2)) is replaced by the generalized Ohm's law (e.g., Braginskii 1965),

$$\boldsymbol{E} + \boldsymbol{v} \times \boldsymbol{B} = \eta \boldsymbol{J} + \eta_{\rm H}\left(\boldsymbol{J} \times \frac{\boldsymbol{B}}{|\boldsymbol{B}|}\right) + \eta_{\rm A}\boldsymbol{J}_\perp, \tag{A1}$$

where $\boldsymbol{J}_\perp$ is the current perpendicular to the magnetic field. The three terms in the r.h.s of Equation (A1) are the magnetic dissipation of the ohmic, Hall, and ambipolar terms, respectively. The coefficients are formulated as follows:

$$\eta = \frac{m_e(\nu_{\rm ei} + \nu_{\rm en})}{4\pi e^2 n_e}, \tag{A2}$$

$$\eta_{\rm H} = \frac{|\boldsymbol{B}|}{4\pi e n_e}, \tag{A3}$$

$$\eta_{\rm A} = \left(\frac{\rho_{\rm n}}{\rho}\right)^2 \frac{|\boldsymbol{B}|^2}{4\pi(\rho_{\rm i}\nu_{\rm in} + \rho_{\rm e}\nu_{\rm en})}, \tag{A4}$$

where indices i, e, n denote the particle species of ion, electron, and neutral hydrogen, respectively. Here, ν_{ab} denotes the collisional frequency of a particle "a" with a particle "b." Collisional frequencies are given by Spitzer (1962) assuming

elastic collision,

$$\nu_{\rm in} = 5 \times 10^{15} x^{-1} n_e \sqrt{\frac{8k_{\rm B}T}{\pi}\frac{m_i + m_n}{m_i m_n}}, \quad \text{(A5)}$$

$$\nu_{\rm en} = 10^{15} x^{-1} n_e \sqrt{\frac{8k_{\rm B}T}{\pi}\frac{m_e + m_n}{m_e m_n}}, \quad \text{(A6)}$$

$$\nu_{\rm ei} = \frac{(4\pi)^2 e^4 \ln\Lambda}{3m_e^2} n_e \left[\frac{m_e}{2\pi k_B T}\right]^{\frac{3}{2}}, \quad \text{(A7)}$$

where the Coulomb logarithm $\ln\Lambda$ is about one order of magnitude. The electron–neutron collision is not effective, $\nu_{\rm en}/\nu_{\rm ei} \sim 0.52/\ln\Lambda(10^4/x)(T/10^3\,{\rm K})^2 < 1$. In dense gas, $\nu_{\rm in} = 3.5 \times 10^{13}\rho_n$ is often used (Draine et al. 1983).

The magnetic Reynolds number ($R_{\rm M} \equiv LV/\eta$) is defined as the ratio of the $|\boldsymbol{v} \times \boldsymbol{B}|$ term to the dissipation term in Equation (A1). We adopt the typical advection scale, $L \sim 1$ pc and $v \sim v_{\rm A} \sim 10$ km s^{-1}, and the magnetic Reynolds numbers in each dissipation are,

$${\rm Re_M} \sim 5.43 \times 10^{14}\left(\frac{x}{10^{-4}}\right)^{3/2}\left(\frac{\beta}{0.01}\right)^{-1/2}\left(\frac{B}{1{\rm mG}}\right)^{-1} \times \left(\frac{n_n}{10^4{\rm cm}^{-3}}\right)^{1/2}\left(\frac{V}{10\ {\rm km\ s}^{-1}}\right)\left(\frac{L}{1\ {\rm pc}}\right), \quad \text{(A8)}$$

$${\rm Re_{M,H}} \sim 8.5 \times 10^{8}\left(\frac{x}{10^{-4}}\right)\left(\frac{B}{1{\rm mG}}\right)^{-1} \times \left(\frac{n_n}{10^4\ {\rm cm}^{-3}}\right)\left(\frac{V}{10\ {\rm km\ s}^{-1}}\right)\left(\frac{L}{1\ {\rm pc}}\right), \quad \text{(A9)}$$

$${\rm Re_{M,A}} \sim 37.9\left(\frac{x}{10^{-4}}\right)\left(\frac{B}{1{\rm mG}}\right)^{-2} \times \left(\frac{n_n}{10^4{\rm cm}^{-3}}\right)^{2}\left(\frac{V}{10\ {\rm km\ s}^{-1}}\right)\left(\frac{L}{1\ {\rm pc}}\right). \quad \text{(A10)}$$

Equations (A8) and (A9) imply that we can ignore the ohmic and Hall dissipation. The ambipolar diffusion may be important for very strong magnetic fields (e.g., $\gg$1 mG) and/or diffuse media ($n_n < 100$ cm^{-3}), expected for high ionization, e.g., $x \gtrsim 10^{-4}$.

ORCID iDs

Yuki Kudoh https://orcid.org/0000-0003-0548-1766
Keiichi Wada https://orcid.org/0000-0002-8779-8486
Colin Norman https://orcid.org/0000-0002-5222-5717

References

Acheson, D. J. 1979, SoPh, 62, 23
Bai, X.-N., & Stone, J. M. 2013, ApJ, 767, 30
Balbus, S. A., & Hawley, J. F. 1991, ApJ, 376, 214
Beckwith, K., Armitage, P. J., & Simon, J. B. 2011, MNRAS, 416, 361
Begelman, M. C., Armitage, P. J., & Reynolds, C. S. 2015, ApJ, 809, 118
Begelman, M. C., & Pringle, J. E. 2007, MNRAS, 375, 1070
Blondin, J. M. 1994, ApJ, 435, 756
Braginskii, S. I. 1965, RvPP, 1, 205
Chan, C.-H., & Krolik, J. H. 2016, ApJ, 825, 67
Chan, C.-H., & Krolik, J. H. 2017, ApJ, 843, 58
Crocker, R. M., Jones, D. I., Melia, F., Ott, J., & Protheroe, R. J. 2010, Natur, 463, 65
Dedner, A., Kemm, F., Kröner, D., et al. 2002, JCoPh, 175, 645
Dorodnitsyn, A., & Kallman, T. 2017, ApJ, 842, 43
Draine, B. T., Roberge, W. G., & Dalgarno, A. 1983, ApJ, 264, 485
Ferrière, K. 2009, A&A, 505, 1183
Flock, M., Dzyurkevich, N., Klahr, H., Turner, N., & Henning, T. 2012, ApJ, 744, 144
Fragile, P. C., & Sądowski, A. 2017, MNRAS, 467, 1838
Han, J. L. 2017, ARA&A, 55, 111
Hawley, J. F., Guan, X., & Krolik, J. H. 2011, ApJ, 738, 84
Hawley, J. F., Richers, S. A., Guan, X., & Krolik, J. H. 2013, ApJ, 772, 102
Hogg, J. D., & Reynolds, C. S. 2016, ApJ, 826, 40
Hsieh, P.-Y., Koch, P. M., Kim, W.-T., et al. 2018, ApJ, 862, 150
Izumi, T., Wada, K., Fukushige, R., Hamamura, S., & Kohno, K. 2018, ApJ, 867, 48
Jiang, Y.-F., Stone, J. M., & Davis, S. W. 2019, ApJ, 880, 67
Kudoh, Y., & Wada, K. 2018, Galax, 6, 139
Kulsrud, R. M. 2005, Plasma Physics for Astrophysics (Princeton, NJ: Princeton Univ. Press)
Liu, H. B., Ho, P. T. P., Wright, M. C. H., et al. 2013, ApJ, 770, 44
Lopez-Rodriguez, E., Packham, C., Jones, T. J., et al. 2015, MNRAS, 452, 1902
Machida, M., Matsumoto, R., Nozawak, S., et al. 2009, PASJ, 61, 411
Machida, M., Nakamura, K. E., Kudoh, T., et al. 2013, ApJ, 764, 81
Matsumoto, Y., Asahina, Y., Kudoh, Y., et al. 2019, PASJ, 71, 83
Meijerink, R., & Spaans, M. 2005, A&A, 436, 397
Mishra, B., Begelman, M. C., Armitage, P. J., & Simon, J. B. 2020, MNRAS, 492, 1855
Miyoshi, T., & Kusano, K. 2005, JCoPh, 208, 315
Modjaz, M., Moran, J. M., Kondratko, P. T., & Greenhill, L. J. 2005, ApJ, 626, 104
Namekata, D., & Umemura, M. 2016, MNRAS, 460, 980
Netzer, H. 2015, ARA&A, 53, 365
Nishiyama, S., Hatano, H., Tamura, M., et al. 2010, ApJL, 722, L23
Nishiyama, S., Yasui, K., Nagata, T., et al. 2013, ApJL, 769, L28
O'Neill, S. M., Reynolds, C. S., Miller, M. C., & Sorathia, K. A. 2011, ApJ, 736, 107
Parkin, E. R., & Bicknell, G. V. 2013, ApJ, 763, 99
Salvesen, G., Armitage, P. J., Simon, J. B., & Begelman, M. C. 2016a, MNRAS, 460, 3488
Salvesen, G., Simon, J. B., Armitage, P. J., & Begelman, M. C. 2016b, MNRAS, 457, 857
Spitzer, L. 1962, Physics of Fully Ionized Gases (New York: Interscience)
Stone, J. M., & Pringle, J. E. 2001, MNRAS, 322, 461
Suresh, A., & Huynh, H. T. 1997, JCoPh, 136, 83
Suzuki, T. K., Fukui, Y., Torii, K., Machida, M., & Matsumoto, R. 2015, MNRAS, 454, 3049
Wada, K. 2012, ApJ, 758, 66
Wada, K., Fukushige, R., Izumi, T., & Tomisaka, K. 2018, ApJ, 852, 88
Wada, K., Papadopoulos, P. P., & Spaans, M. 2009, ApJ, 702, 63
Wada, K., Schartmann, M., & Meijerink, R. 2016, ApJL, 828, L19
Yokoyama, T., & Shibata, K. 1994, ApJL, 436, L197
Zhu, Z., & Stone, J. M. 2018, ApJ, 857, 34